Atmos. Chem. Phys. Discuss., 13, 9217–9265, 2013
www.atmos-chem-phys-discuss.net/13/9217/2013/
doi:10.5194/acpd-13-9217-2013

Atmospheric Chemistry and Physics Discussions

Turbulent collision-coalescence in maritime shallow convection

A. A. Wyszogrodzki[1], W. W. Grabowski[1], L.-P. Wang[2], and O. Ayala[2,3]

[1]National Center for Atmospheric Research, Boulder, Colorado, USA
[2]Department of Mechanical Engineering, University of Delaware, Newark, Delaware, USA
[3]Department of Engineering Technology, Old Dominion University, Norfolk, Virginia, USA

Received: 4 February 2013 – Accepted: 19 March 2013 – Published: 8 April 2013

Correspondence to: W. W. Grabowski (grabow@ncar.ucar.edu)

Published by Copernicus Publications on behalf of the European Geosciences Union.

Abstract

This paper discusses cloud simulations aiming at quantitative assessment of the effects of cloud turbulence on rain development in shallow ice-free convective clouds. Cloud fields from large-eddy simulations (LES) applying the bin microphysics with the collision kernel enhanced by cloud turbulence are compared to those with the standard gravitational collision kernel. Simulations for a range of cloud condensation nuclei (CCN) concentrations are contrasted. Details of the turbulent kernel and how it is used in LES simulations are presented. Because of the disparity in spatial scales between the bottom-up numerical studies guiding the turbulent kernel development and the top-down LES simulations of cloud dynamics, we address the consequence of the turbulence intermittency in the unresolved range of scales on the mean collision kernel applied in LES. We show that intermittency effects are unlikely to play an important role in the current simulations. Highly-idealized single-cloud simulations are used to illustrate two mechanisms that operate in cloud field simulations. First, the microphysical enhancement leads to earlier formation of drizzle through faster autoconversion of cloud water into drizzle, as suggested by previous studies. Second, more efficient removal of condensed water from cloudy volumes when a turbulent collection kernel is used leads to an increased cloud buoyancy and enables clouds to reach higher levels. This is the dynamical enhancement. Both mechanisms seem to operate in the cloud field simulations. The microphysical enhancement leads to the increased drizzle and rain inside clouds in simulations with high CCN. In low-CCN simulations with significant surface rainfall, dynamical enhancement allows maintenance of the cloud water path despite significant increase of the precipitation water path and dramatically increased mean surface rain accumulation. These results call for future modeling and observational studies to corroborate the findings.

ACPD
13, 9217–9265, 2013

1 Introduction

Cloud droplets grow by the diffusion of water vapor up to sizes where collision-coalescence among the droplets begins to move the condensed water into drizzle drops and eventually into rain drops. Observed rapid onset of rain in shallow clouds in the tropics and subtropics is often difficult to explain applying the classical droplet growth theory, and several mechanisms that may accelerate the onset have been considered in the past. These include the impact of giant and ultra-giant cloud condensation nuclei (CCN) that can grow by the water vapor diffusion into drizzle sizes, cloud entrainment (that can lead to a significant broadening of the cloud droplet spectrum in diluted volumes and thus promote droplet collisions), and effects of cloud turbulence. The latter includes the effects on relative motion of droplets, concentration fluctuations, and collision efficiencies (Khain et al., 2000; Franklin et al., 2005; Wang et al., 2005). The rate of droplet collisions is controlled by the gravitational mechanism for drizzle/rain drops of radii larger than 50 µm, but air turbulence can significantly enhance the collision rate for cloud droplets with radii between 10 and 30 µm and for intermediate droplets/drops with radii between 30 to 50 µm (Grabowski and Wang, 2013).

Effects of air turbulence on geometric collision rates and on collision efficiency have been studied applying the direct numerical simulation (DNS), and accounting for the droplet-size dependence (which in turn determines the response time and settling velocity), the strength of air turbulence (i.e. the dissipation rate, Reynolds number, etc.), the gravity force acting on the droplets, and interactions of droplets with the air turbulence (e.g. Franklin et al., 2005; Wang et al., 2005, 2006b; Ayala et al., 2008a, b). The effects of turbulence on the collection kernel could include increased relative motion due to differential acceleration and shear effects (Wang et al., 2000; Zhou et al., 2001), the increased average pair density due to local concentration enhancement (Wang et al., 2000; Zaichik and Alipchenkov, 2003; Zaichik et al., 2003), selective alterations of the settling rate by turbulence (Wang and Maxey, 1993; Davila and Hunt, 2001), and enhanced collision efficiency (Pinsky et al., 1999; Wang et al., 2005, 2008; Ayala et al.,

ACPD
13, 9217–9265, 2013

2007). Many questions remain to be answered regarding the true quantitative level of the above effects (Grabowski and Wang, 2013).

Wang et al. (2005) developed a general kinematic formulation that describes the droplet collision kernel in turbulent air with hydrodynamic interactions and gravitational settling. One way to formulate a turbulent collision kernel is to combine a turbulent geometric collision kernel (Ayala et al., 2008b), gravitational collision efficiency (Hall, 1980), and a collision-efficiency enhancement factor by air turbulence (Wang et al., 2008). A hybrid direct numerical simulation (HDNS, Ayala et al., 2007) has been used to study the turbulent geometric collision kernel and the collision-efficiency enhancement factor in Wang et al. (2005, 2008), Ayala et al. (2008a). Ayala et al. (2008b) developed a comprehensive theory for turbulent geometric collision kernel, which was used in Xue et al. (2008) to study the impact of air turbulence on warm rain initiation. It was found that the air turbulence can accelerate the growth of cloud droplets by speeding up the autoconversion phase, thus shorten the time for the formation of drizzle drops by up to 40 % relative to the Hall gravitational collection kernel (Xue et al., 2008; Grabowski and Wang, 2009).

The complexity of droplet interactions with the turbulent flow and limitations of cloud measurements result in uncertain estimates of the level of collision-rate enhancement by air turbulence (Grabowski and Wang, 2013). Additional effects can also widen the droplet spectrum and promote collisional growth. For instance, CCN differences in marine and continental environments are primarily responsible for microphysical differences between clean and polluted clouds (Pruppacher and Klett, 1997). Moreover, for a given cloud, updraft strength varies significantly across the cloud base and affects the number of activated droplets. Finally, in shallow cumuli, CCN are activated above the cloud base and lead to the observed approximately constant-with-height mean concentration of cloud droplets despite a significant dilution of such clouds by entrainment (e.g. Slawinska et al., 2012; Wyszogrodzki et al., 2011).

In this paper, we focus on the effects of turbulent acceleration of rain formation in a field of simulated shallow cumulus clouds. Since rain development depends on the

ACPD
13, 9217–9265, 2013

cloud depth as well as on the CCN characteristics, we perform a set of model simulations varying CCN characteristics and analyze the results in such a way that the effects of turbulence are unambiguously evaluated. Cloud field simulations applying either gravitational or turbulent collection kernels are compared. We apply a large-eddy simulation (LES) fluid flow model (used previously in LES bulk microphysics simulations discussed in Grabowski, 2007; Jarecka et al., 2009; Slawinska et al., 2012) coupled to the bin microphysics scheme used in studies reported in Grabowski and Wang (2009), Grabowski et al. (2011) and Wyszogrodzki et al. (2011). Our study is similar to the one reported in Seifert et al. (2010) except that we apply a bin microphysics scheme rather than a double-moment bulk scheme used in Seifert et al. (2010). Formulation of the turbulent enhancement of the traditional gravitational collection kernel is discussed in the next section. Because of computational limitations, a LES model gridbox has to be significantly larger than the volume of the computational domain applied in DNS studies guiding the development of the turbulent collection kernel. It follows that the intermittency of the dissipation rate in the physical space needs to be considered before the enhancement is applied in the LES study. This aspect is discussed in Sect. 3. Section 4 provides a brief description of the LES model and details of the model setup. Model results are discussed in Sect. 5. A brief summary in Sect. 6 concludes the paper.

2 Formulation of gravitational and turbulent collection kernels

The impact of turbulent collisions on warm-rain processes is evaluated by comparing simulations that apply the turbulent collection kernel with simulations using the classical gravitational kernel. The gravitational collection kernel is given by:

$$K_{ij} = \pi\,(a_i + a_j)^2\,|v_i^t - v_j^t|E_{ij}^g \qquad (1)$$

where E_{ij}^g is the gravitational collision efficiency of droplets with radii a_i and a_j in a quiescent background air, and v_i^t and v_j^t are droplet sedimentation (terminal) velocities.

ACPD
13, 9217–9265, 2013

Collision efficiencies are obtained by linearly interpolating tabulated values given in Hall (1980). Terminal velocities are prescribed according to Beard (1976) as given in Pruppacher and Klett (1997).

The turbulent collision/collection kernel combines the analytical parameterization of the turbulent geometric collection kernel of Ayala et al. (2008b) with the collision-efficiency enhancement factor obtained from HDNS (Wang et al., 2005, 2008; Ayala et al., 2007). Namely, the turbulent collection kernel is expressed as:

$$K_{ij} = K_{ij}^{tg}\, E_{ij}^{g}\, \eta_E \tag{2}$$

where the turbulent geometric collection kernel K_{ij}^{tg} is obtained when droplet-droplet local aerodynamic interaction is not considered. In this case, the disturbance flows induced by other droplets are excluded when the motion of a given droplet is solved. The collision efficiency of droplets in a quiescent background air E_{ij}^{g} is as in Eq. (1). The ratio of turbulent collision efficiency to E_{ij}^{g} is represented by the relative enhancement factor η_E (Wang et al., 2005) which depends on the flow dissipation rate ϵ. The collision-efficiency enhancement factor η_E is interpolated from the hybrid DNS data for two intensities of turbulence (ϵ of 100 and 400 $\mathrm{cm^2\,s^{-3}}$ shown in Table 1. Assuming $\eta_E = 1$ for $\epsilon = 0$, the enhancement factors for other dissipation rates are derived by either interpolation or extrapolation. Specifically, we follow an approach used in Seifert et al. (2010) and calculate η_E as follows:

- for $0 \le \epsilon \le 100\,\mathrm{cm^2\,s^{-3}}$, a linear interpolation between $\eta_E = 1$ for $\epsilon = 0$ and the value of η_E for $\epsilon = 100\,\mathrm{cm^2\,s^{-3}}$ is used;
- for $100 < \epsilon \le 400\,\mathrm{cm^2\,s^{-3}}$, a linear interpolation between the values of η_E at $\epsilon =$ 100 $\mathrm{cm^2\,s^{-3}}$ and $\epsilon = 400\,\mathrm{cm^2\,s^{-3}}$ is used;
- for $400 < \epsilon \le 600\,\mathrm{cm^2\,s^{-3}}$, a linear extrapolation from the values of η_E at $\epsilon =$ 100 $\mathrm{cm^2\,s^{-3}}$ and $400\,\mathrm{cm^2\,s^{-3}}$ is used;

ACPD
13, 9217–9265, 2013

– for $\epsilon > 600\,\mathrm{cm^2\,s^{-3}}$, the extrapolated value at $\epsilon = 600\,\mathrm{cm^2\,s^{-3}}$ is used.

The turbulent geometric collection kernel K_{ij}^{tg} is given by the kinematic formulation (Wang et al., 2005):

$$K_{ij}^{tg} = 2\pi R^2 \langle |w_r(r=R)| \rangle\, g_{ij}(r=R) \tag{3}$$

where $R = a_i + a_j$ is the geometric collision radius, the radial relative velocity w_r is defined in terms of the center-to-center separation vector $\boldsymbol{r}$ (pointing from a droplet of radius a_j to a droplet of radius a_i), the velocity V_i of the a_i droplet, and the velocity V_j of the a_j droplet as:

$$w_r = \boldsymbol{r} \cdot (V_i - V_j)/r \tag{4}$$

with $r = |\boldsymbol{r}|$. The additional factor g_{ij} is the radial distribution function that measures the effect of preferential concentration on the pair number density at separation $r = R$. Both $\langle |w_r| \rangle$ and g_{ij} in (3) are computed without local aerodynamic interaction. The kinematic formulation (3) has been validated against dynamic collision rates from DNS/HDNS for both ghost droplets and aerodynamically-interacting droplets in a turbulent air flow, see Wang et al. (2005) and Ayala et al. (2008a). Ayala et al. (2008b) developed parameterizations for both $\langle |w_r| \rangle$ and g_{ij}, guided by DNS data. It should be noted that their parameterizations consider the effects of flow Reynolds number which cannot be fully represented by HDNS. For example, the parameterization for $\langle |w_r| \rangle$ makes use of velocity correlations that are valid for both the dissipation subrange and the energy-containing subrange of turbulence. The intermittency of small-scale turbulent fluctuations was incorporated into the model for g_{ij} following Chun et al. (2005). The detailed expression for K_{ij}^{tg}, and g_{ij} can be found in Ayala et al. (2008b) and in the appendix of the current paper.

ACPD
13, 9217–9265, 2013

3 Effects of the dissipation intermittency on the turbulent collection kernel

Due to computational limitations, the HDNS domain size is currently limited to about 1 m or less, and only the sub-dissipation and dissipation scales as well as a limited range of inertial-range scales can be explicitly resolved. The underlying assumption in HDNS is that the pair-statistics relevant to turbulent collision-coalescence are governed mostly by the dissipation range scales because the droplet Stokes number (i.e. the ratio between the droplet inertial response time and the flow Kolmogorov time) is typically on the order of one or less. Such a HDNS domain size is significantly smaller than the typical gridlength (10–100 m) in atmospheric LES targeting clouds. The limited domain size implies a limited Taylor microscale Reynolds number, ~ 500 or less. This is one to two orders of magnitude lower than what is found in cumulus clouds.

Because of these limitations, there are two general issues that must be resolved. First, one must ensure that the HDNS-guided collection kernel is independent of the domain size and the large-scale forcing algorithm. Indeed, for droplets smaller than $\sim 30\,\mu$m in radius, such a convergence has been demonstrated (Rosa et al., 2011, 2013). The parameterization of the turbulent geometric collision kernel of Ayala et al. (2008b) applies a description of the two-point two-time fluid velocity correlation that is valid for much higher flow Reynolds numbers than in HDNS. This partially removes the limitation of the small flow Reynolds number in HDNS. However, larger droplets have larger settling velocity, and the crossing-trajectory effect combined with droplet inertia could imply a larger range of flow scales affecting the pair relative statistics. HDNS data at higher resolutions and larger domain sizes are still needed to validate the theoretical parameterization.

The second issue concerns increasing intermittency of the local dissipation rate with increasing flow Reynolds number. It is well known that the local flow dissipation rate takes more extreme values in small regions when the flow Reynolds number is increased. This is reflected in the higher velocity derivative flatness and more extended tail in PDF of the local dissipation rate and local fluid acceleration (e.g. Sreenivasan

ACPD
13, 9217–9265, 2013

and Antonia, 1997; Pinsky and Khain, 2004). Since the local collision kernel depends on the local flow dissipation, a question arises as to whether the different levels of flow intermittency in DNS computational domain and LES grid volume affect the average collision kernel. In practical terms, the LES gridbox consists of thousands to millions of DNS domains, with a distribution of eddy dissipation rates in each DNS domain that average out to the mean dissipation rate of the LES gridbox. Since the turbulent collision kernel derived from HDNS is nonlinear in the dissipation rate, simply using the collision kernel based on the LES-derived average dissipation rate may not yield the same answer as averaging DNS kernels with the distribution of the dissipation rates.

More specifically, the latter issue can be formulated as follows. Let l_1 be the HDNS domain size and l_2 be the gridlength in LES, with $l_2 > l_1$ and both l_1 and l_2 falling into the inertial subrange. Moreover, let ϵ_1 and ϵ_2 denote the flow dissipation rate averaged over a volume of size l_1 and l_2, respectively. If the collision kernel derived from HDNS is $K_{ij}(\epsilon_1, u',)$, then the average collision kernel in the LES grid volume, taking into account of the dissipation intermittency, can be expressed as

$$\langle K_{ij} \rangle \equiv \int K_{ij}(\epsilon_1, u'(l_2, \epsilon_1),) f\left(\ln \frac{\epsilon_1}{\epsilon_2}; \frac{l_2}{l_1}\right) d \ln \frac{\epsilon_1}{\epsilon_2}, \tag{5}$$

where $f(\ln \epsilon_1/\epsilon_2; l_2/l_1)$ is the PDF of $\ln \epsilon_1/\epsilon_2$ for a given l_2/l_1, and in the integrand u' is estimated by $u' \approx (2\epsilon_1 l_2)^{1/3}$. There are two reasons why l_2 is used in estimating u'. First, the collision kernel is contributed by both resolved and subgrid velocity fluctuations in the LES grid box. Second, K_{ij} inside the integrand is a derived model already extending the level of velocity fluctuations in the HDNS domain to the level of velocity fluctuations in clouds, and the only aspect that was not modeled is the added intermittency of the local dissipation rate at cloud Reynolds numbers.

The Kolmogorov refined similarity theory (Kolmogorov, 1962) implies that the PDF of f is Gaussian with a variance of $\sigma_{ij}^2 = \mu \ln(l_2/l_1)$, where μ is a universal parameter. The mean of the distribution can be determined then by the fact that the mean of ϵ_1

ACPD
13, 9217–9265, 2013

according to the prescribed PDF is ϵ_2. Therefore, the PDF takes the following form:

$$f\left(\ln\frac{\epsilon_1}{\epsilon_2};\frac{l_2}{l_1}\right)=\frac{1}{\sqrt{2\pi}\sigma_{12}}\exp\left\{-\frac{\left[\ln(\epsilon_1/\epsilon_2)+\sigma_{12}^2/2\right]^2}{2\sigma_{12}^2}\right\}, \tag{6}$$

where the following consistency condition is enforced

$$\int_0^\infty \epsilon_1 f\left(\ln\frac{\epsilon_1}{\epsilon_2}\right) d(\ln\frac{\epsilon_1}{\epsilon_2})=\epsilon_2. \tag{7}$$

A review of experimental data (Sreenivasan and Kailasnath, 1993) shows that the intermittency exponent μ takes a value of $\mu = 0.25 \pm 0.05$, so the PDF is now completely specified in terms of ϵ_2/ϵ_1 and l_2/l_1 ratios. This formulation provides a method to evaluate the effect of dissipation intermittency on $K_{ij}(\epsilon_2, u')$. Specifically, we ask whether the ratio

$$\mathcal{R}\left(\frac{l_2}{l_1},\epsilon_2\right)=\frac{\langle K_{ij}\rangle}{K_{ij}(\epsilon_2,u'(l_2,\epsilon_2))} \tag{8}$$

is close to one or not.

Using the formulation provided in the Appendix, we performed a numerical integration to obtain $\mathcal{R}$, for different droplet radii a_i and a_j, the ratio l_2/l_1, and ϵ_2.

Figure 1 shows the contours of $\mathcal{R}$ for two typical dissipation rates and $l_2/l_1 = 50$. For most droplet size combinations, $\mathcal{R}$ is slightly less than one, implying that the dissipation intermittency *reduces* the effect of turbulence. This can be understood as follows. Pair statistics relevant to collision-coalescence are second-order statistics and they tend to be dominated by regions of low flow dissipation rates which occupy most of the space. Increasing the intermittency implies a slight increase in the probability of the low

ACPD
13, 9217–9265, 2013

dissipation-rate regions when the mean dissipation rate is fixed, and the higher dissipation rates take more extreme values. Furthermore, the extreme-dissipation regions occupy a small fraction of the volume, and their impact on the mean collision kernel is outweighed by the reduced kernel in low-dissipation regions.

Pinsky and Khain (2004) showed that a more realistic (i.e. non-Gaussian) PDF of flow accelerations actually reduced the value of radial relative velocity by 10 to 15 % when compared to a Gaussian PDF. This level of reduction is quite similar to what are shown in Fig. 1 for $\epsilon_2 = 500\,\mathrm{cm}^2\,\mathrm{s}^{-3}$. There are also some droplet-size combinations where $\mathcal{R}$ is slightly larger than one, which could be a result of enhanced inertial clustering by intermittent flow events.

In Fig. 2, we plot $\mathcal{R}$ as a function of the flow dissipation rate for $l_2/l_1 = 10$ and 1000 for some typical droplet size combinations. In general, there is an increasing deviation from one as ϵ_2 is increased. However, for small and intermediate dissipation rates, $\mathcal{R}$ does not deviate significantly from one (i.e. the difference is below 10 %). The fact the $\mathcal{R}$ does not deviate significantly from unity for a wide range of eddy dissipation rates and cloud droplet sizes, together with inherent limitations of the LES approach, suggests that the effect of dissipation intermittency due to the size gap between DNS and LES may be neglected, at least until more confident estimations of the turbulent enhancement are obtained and higher spatial resolution of bin-microphysics LES simulations becomes feasible.

4 EULAG LES model with bin microphysics and effects of cloud turbulence

4.1 The model and setup of model simulations

The LES model with bin microphysics is the same as in Wyszogrodzki et al. (2011; WGW11 hereafter) except that it is extended to include a representation of droplet growth by collision-coalescence. The fluid flow is calculated by the anelastic EULAG model (see Prusa et al., 2008 for a review and comprehensive list of references).

ACPD
13, 9217–9265, 2013

The flow model is combined with the size-resolving representation of warm-rain microphysics that includes droplet activation and growth by water vapor diffusion and by collision-coalescence as described in Grabowski and Wang (2009) and Grabowski et al. (2011). The bin microphysics applies the linear flux method of Bott (1998) to calculate growth by collision-coalescence. The number of bins in the microphysics scheme was selected as $\mathcal{N} = 112$, which – together with the improved representation of the droplet activation – resulted in almost converged numerical solutions as shown in Grabowski et al. (2011).

We consider simulations of a field of shallow cumuli based on the Barbados Oceanographic and Meteorological Experiment (BOMEX; Holland and Rasmusson, 1973) and used in the model intercomparison study described in Siebesma et al. (2003). EULAG application to the BOMEX case with either single-moment or double-moment bulk microphysics was reported in Grabowski (2006), Jarecka et al. (2009, 2011), Slawinska et al. (2012), and WGW11. Figure 3 presents initial zonal wind (meridional wind is assumed zero), temperature, and moisture profiles of the BOMEX setup. The profiles show the 1-km-deep trade-wind convection layer overlaying the 0.5 km-deep mixed layer near the ocean surface. The convection layer is covered by 0.5 km-deep trade-wind inversion. The quasi-steady conditions are maintained by the prescribed large-scale subsidence, large-scale moisture advection, surface heat fluxes, and radiative cooling. The original BOMEX case considers nonprecipitating convection, but we extend it here by adding precipitation processes. With precipitation, the steady-state conditions of the original setup may evolve in time, an aspect not explored in the current study.

Details of the model setup are exactly as in WGW11, with horizontal/vertical gridlength of $\Delta x = \Delta y = 50\,\mathrm{m}$, $\Delta z = 20\,\mathrm{m}$. The model time step varies between 0.5 and 1.5 s depending on the strength of convection. The model is run for 6 h and two types of results are collected: (i) horizontally- and one-minute averaged statistics from the entire simulation for selected fields (e.g. cloud water mixing ratio, rain rate, etc.), and (ii) three-dimensional snapshots from the last 3 h collected every 5 min. Since the pri-

ACPD
13, 9217–9265, 2013

mary factor affecting the ability of an ice-free cloud to precipitate is the concentration of aerosol particles serving as CCN, we consider a range of CCN concentrations by applying a general droplet activation formula in the form:

$$N_{CCN} = \begin{cases} N^0_{CCN} & \text{for } S > 1 \\ N^0_{CCN}\, S^{0.4} & \text{for } 0.1 < S < 1 \\ N^0_{CCN}\, (0.1)^{-3.6} S^4 & \text{for } S < 0.1 \end{cases} \quad (9)$$

with S in % and N^0_{CCN} values of 30, 60, 120, and 240 mg^{-1}. Such a range represents extremely clean to weakly polluted cloud conditions for subtropical shallow convective clouds. Simulations with the range of CCN concentrations will be referred to as $N30$, $N60$, $N120$, and $N240$. For each CCN conditions, three sets of simulations were performed: (i) without collision-coalescence (i.e. as in WGW11), (ii) with collision-coalescence applying the gravitational collection kernel, and (iii) with collision-coalescence and turbulent enhancement of droplet collisions based on local characteristics of cloud turbulence.

As an example, Fig. 4 presents snapshots of the 3-D distribution of cloud fields at a time of 6 h for the $N120$ case, marking cloudy volumes with cloud water mixing ratio $q_c > 0.05$ g kg^{-1} with transparent gray color, and the rain water areas (blue color) for rain water mixing ratio $q_r > 0.1$ g kg^{-1}. To calculate cloud and rain water mixing ratios, the spectrum of drops is divided between the cloud and drizzle/rain assuming the drop threshold radius of 25 µm. The figure shows that several clouds, shallow and relatively deep, are present in the computational domain. They are at different stages of their lifecycle, some precipitating and some not. In agreement with previous studies (e.g. Siebesma et al., 2003; Slawinska et al., 2012) the cloud coverage is typically around 10 %.

ACPD
13, 9217–9265, 2013

4.2 Turbulent enhancement of the collection kernel in LES model

Because of relatively coarse resolution of the LES simulations, turbulent processes within simulated clouds remain mostly parameterized. In particular, the model solves a prognostic equation for the turbulent kinetic energy (TKE) as described in Margolin et al. (1999) with parameters adopted from Schumann (1991). The grid-volume averaged dissipation rate ϵ is derived from TKE as

$$\epsilon = C_{\mathrm{eps}}(\mathrm{TKE})^{3/2}/\Delta \tag{10}$$

where $\Delta = (\Delta x + \Delta y + \Delta z)/3$ is the arithmetic average of model grid increments, and $C_{\mathrm{eps}} = 0.845$. The flow Reynolds number Re_λ is defined using the root-mean-square (rms) velocity u_{rms} as (Pope, 2000; Wang et al., 2006a)

$$Re_\lambda = 15^{1/2}(u_{\mathrm{rms}}/v_{\mathrm{K}})^2 \tag{11}$$

where v_{K} is the Kolmogorov velocity. The rms velocity is derived assuming that $\epsilon \sim u_{\mathrm{rms}}^3$ and selecting $u_{\mathrm{rms}} = 2.02\,\mathrm{m\,s^{-1}}$ for $\epsilon = 400\,\mathrm{cm^2\,s^{-3}}$. This gives an empirical formula for u_{rms} (in $\mathrm{m\,s^{-1}}$) in the form (Wang et al., 2006a):

$$u_{\mathrm{rms}} = 2.02 \cdot (\epsilon/400.)^{1/3} \tag{12}$$

with ϵ expressed in $\mathrm{cm^2\,s^{-3}}$. For small droplets, the collision kernel is not affected by u_{rms}, while for larger droplets, u_{rms} (or Re_λ) has a secondary effect on the kernel. Overall, the increase of TKE (and thus ϵ, u_{rms}, and Re_λ) shortens the time needed to form drizzle drops. The growth times also depend on the liquid water content (LWC), but the relative reduction of the growth time for a given dissipation rate is similar for different LWCs due to the self-similarity of the kinetic collection equation.

ACPD
13, 9217–9265, 2013

5 Results

5.1 Preamble: rising thermal simulations

We start with a brief discussion of results of more idealized (2-D single-cloud) simulations that help understanding effects of turbulence on warm-rain formation in realistic cloud-field simulations. We apply the idealized model setup previously considered in Grabowski et al. (2010; Sect. 5). In this setup, an initially circular moist warm thermal (a bubble) rises in the stratified environment and forms a cloud. As cloud droplets grow by the diffusion of water vapor and eventually by collision-coalescence, drizzle and rain develop, with rain falling out of the cloud and reaching the surface. Removal of cloud water from the cloud and mixing with subsaturated cloud environment leads to cloud dissipation and rain cessation.

For reasons that will become obvious while discussing the results, we consider two model setups featuring different environmental conditions. The first setup (upper panels on Fig. 5) is exactly as Grabowski et al. (2010) and features two layers in two halves of the domain vertical extent. The lower/upper layer features static stability of $1.3/3.0 \times 10^{-5}\,\mathrm{m}^{-1}$. In this setup, the initial perturbation rises across the lower layer, but its further vertical development is arrested by the presence of the more stable upper layer (see Fig. 8 in Grabowski et al., 2010). The second setup (lower panels on Fig. 5) assumes a single-layer atmospheric structure, with the static stability of $1.6 \times 10^{-5}\,\mathrm{m}^{-1}$ and relative humidity of 80 %. An initial perturbation, the same as in Grabowski et al. (2010), rises across the domain and reaches levels close to the upper model boundary (at 5 km) near the end of these simulations. Two simulations are performed for each model setup applying EULAG with the same bin microphysics scheme as in cloud field simulations. The first simulation applies the gravitational collision kernel. The second simulation includes effects of cloud turbulence in an extremely simplified way, namely, by assuming that the turbulence intensity at all cloudy points corresponds to a constant eddy dissipation rate of $\epsilon = 100\,\mathrm{cm}^2\,\mathrm{s}^{-3}$. N^0_{CCN} of $120\,\mathrm{mg}^{-1}$ is assumed in (9) for all four simulations.

ACPD
13, 9217–9265, 2013

A synthesis of model results is presented in Fig. 5. The figure shows evolution of the height of the cloud water center of mass (the barycenter) and the total accumulated surface precipitation. As expected, thermals in simulations with the inversion rise to approximately similar height as documented by the barycenter height evolutions. The key result is that rain reaches the surface about 4 min earlier in the turbulent case, and there is about 40 % more total accumulated rain in this case. Arguably, the latter comes from earlier (in the cloud lifecycle) formation of initial drizzle drops from cloud droplets through the autoconversion phase of rain formation. This gives more cloud water available throughout the rest of the cloud lifecycle for the accretion phase of the rain development, when existing drizzle and rain drops collect cloud droplets.

When thermals are allowed to rise without the inversion, the difference in the total accumulated rain is even larger, a factor of two. It means that the "microphysical enhancement" (i.e. earlier formation of initial drizzle through the autoconversion phase) is supplemented by an additional mechanism. As the differences in the height of the LWC center of mass suggest, the thermal with turbulent kernel rises to higher levels and provides more condensed water for the rain formation. Arguably, the difference comes from "off-loading" the condensed water through rain formation, more effective when the turbulent kernel is used. Condensed water reduces cloud positive buoyancy and its removal leads to increased buoyancy and thus a possibility of reaching higher levels. This "dynamical enhancement" adds to the microphysical enhancement discussed above and they both result in an astonishing overall effect evident in the lower panels.

One should treat the above results with significant caution. For instance, another aspect of these simulations is that thermals rising without the inversion actually produce less rain at the surface than thermals impinging upon the inversion (compare scales on vertical axes in the right panels; this may be because more rain evaporates during its fall from the cloud to the surface when thermals reach higher levels.) Assumed 2-D geometry, simple cloud forcing (a bubble), and constant in space and time characteristics of the cloud turbulence all make the model results discussed above qualitative.

ACPD
13, 9217–9265, 2013

Nevertheless, the results highlight mechanisms involved, the significance of combined microphysical and dynamical factors in particular. These will play an important role in cloud field simulations presented in subsequent sections.

5.2 Statistics of local cloud properties in cloud field simulations

Figure 6 presents contoured frequency by altitude diagrams (CFADs) of the dissipation rate inside cloudy volumes (left panel), and the adiabatic fraction AF (the ratio between the local LWC and the adiabatic one; right panel) for the *N*120 simulation. Plots for other simulations are similar (not shown). The figure documents features well established from numerous observations and simulations of shallow convection: large variability of local cloud characteristics at a given height, significant cloud dilution with the mean AF decreasing with height, turbulence intensity with typical ϵ values between a fraction of $1\,\mathrm{cm^2\,s^{-3}}$ and a few tens $\mathrm{cm^2\,s^{-3}}$, and the maximum ϵ values reaching several hundreds $\mathrm{cm^2\,s^{-3}}$ in the upper part of the cloud field. One might anticipate formation of initial drizzle drops in volumes featuring high AF and an acceleration of this process if significant levels of cloud turbulence are present. Inspection of cloud field snapshots documents that the highest turbulence intensity typically occurs near cloud edges in upper parts of individual cumuli, and this is where the highest LWC is often found. Such a picture agrees with the discussion in Seifert et al. (2010, see Fig. 6 in particular).

Figure 7 shows percentile distributions of the cloud droplet concentration for the *N*120 with and without collision-coalescence. Results of the simulation without collision-coalescence are similar to those shown in WGW11: distributions are relatively wide with the most frequent concentration values approximately constant with height (except in the uppermost 0.5 km of the cloud field depth). As documented in Slawinska et al. (2012) and WGW11, the almost constant mean droplet concentration as a function of height (also observed in field studies, see discussion in Slawinska et al., 2012) comes from the secondary (i.e. above the cloud base) activation of CCN. Distributions for simulations with collision-coalescence are similar to those without collisions,

ACPD
13, 9217–9265, 2013

except that clouds with turbulent collisions appear reaching higher levels. Overall, the presence of precipitation seems to have only a small impact on CFADs of the droplet concentration.

Figure 8 shows CFADs of the effective radius (the ratio between the third and the second moment of the cloud droplet size distribution) for the *N*120 case. Effective radius, together with the local LWC, determines local cloud properties relevant to the transfer of the solar radiation, and it is typically slightly larger than the mean volume radius (i.e. the radius of the mean mass droplet, the LWC divided by the droplet concentration). The figure also shows profiles of the effective radius for adiabatic monodisperse spectra of cloud droplets corresponding to droplet concentrations of 90, 120, and 150 mg^{-1}. Without collision-coalescence, CFAD of the effective radius is relatively wide, and the maximum frequency is consistent with the adiabatic profiles. With gravitational collision-coalescence, CFAD's frequency maximum begins to shift to the right (i.e. toward larger sizes and lower concentrations) in the upper part of the cloud field. This is barely visible for the gravitational coalescence but becomes obvious when the effects of turbulence are included. For simulations with lower CCN, the shift is apparent even with the gravitational coalescence, but it is barely visible for turbulence-enhanced collisions with the highest CCN concentration considered.

5.3 Rainfall in cloud field simulations

Figures 9 and 10 show evolutions of the horizontally-averaged cloud water and the drizzle/rain water mixing ratios, respectively. The Fig. 9 panels show that the presence of significant drizzle/rain strongly affects mean cloud water profiles in both gravitational and turbulent cases. In low CCN simulations *N*30 and *N*60, cloud water is clearly reduced in the upper part of the cloud field due to its efficient removal by drizzle/rain. The figure also shows oscillations of the cloud field due to interactions between clouds and their environment as well as the random nature of cloud initiation and evolution. Mean cloud water above the cloud base features periods of enhanced horizontally-averaged cloud water that develop from the cloud base upwards as tilted yellow streaks with the

ACPD
13, 9217–9265, 2013

highest mean cloud water (red color) at some of their tops, especially in high-CCN simulations. These oscillations of the mean cloud field are also apparent in the time evolution of the horizontally-averaged drizzle/rain water mixing ratio shown in Fig. 10, with the highest mean drizzle/rain in the upper parts of the cloud field and in periods of enhanced mean cloud water. The amount of drizzle/rain strongly increases with the decrease of CCN concentrations (note different color scales in panels corresponding to various CCN concentrations) as one might expect. Overall, the mean drizzle/rain seems higher when the turbulent kernel is used, an aspect quantified in the subsequent analysis. High drizzle/rain values in the upper parts of the cloud field (red colors) are the initiation points of downward streaks as enhanced rain falls towards the ocean surface.

Figure 11 shows evolutions of the precipitation fraction profiles for all eight simulations. Precipitation fraction is an analog of the cloud fraction, that is, the fraction of the horizontal area covered by clouds at a given height. At each height, precipitation fraction is defined as the fraction of the horizontal domain with precipitation rate larger than $3.65 \times 10^{-5}\,\mathrm{ms}^{-1}$. The specific threshold comes from the estimated cutoff precipitation flux of the precipitation radar, see Sect. 2.4.2 in van Zanten et al. (2010). Because of the fluctuations of cloud and precipitation fields, 1 min precipitation fraction profiles vary significantly. The average profiles, on the other hand, clearly illustrate differences between various simulations, the impact of CCN and turbulent enhancement in particular. In simulations *N*240 (bottom row), precipitation is only present in the upper parts of the cloud field (consistent with Fig. 10), with some downward extension of the mean profile in the turbulent kernel case. In the *N*120 case, precipitation seems to reach the surface only when turbulent collision kernel is considered. In *N*60 and *N*30 cases, a significant increase of the precipitation fraction (factor of two) is simulated with turbulent collisions. It is also apparent that turbulent profiles correspond to a deeper cloud field, with turbulent profiles approaching zero at heights around or above 2.5 km, whereas profiles for the gravitational kernel terminating between 2.2 and 2.3 km. This seems to represent the dynamic enhancement, that is, a more efficient off-loading of cloud condensate

ACPD
13, 9217–9265, 2013

in the case of turbulent kernel. Instead of the precipitation fraction, one may consider profiles of the precipitation flux because its time-averaged surface value represents surface rain accumulation. Such profiles provide a similar message as Fig. 11 and are not shown.

Figure 12 presents the time evolution of the domain-averaged cloud water path (CWP) and precipitation water path (PWP), namely, vertical integrals of the cloud water and drizzle/rain water contents, respectively, for simulations with gravitational and turbulent kernels. CWP and PWP are additionally averaged over 1 min time interval. The figure represents a more comprehensive representation of model results shown in Figs. 9 and 10. CWP (as well as PWP in simulations with significant rain) fluctuates significantly as cloud fields evolve. Simulations *N*240 and *N*120 show similar mean CWP values and little PWP in agreement with the previous discussion. In contrast, simulations *N*60 and *N*30 show significant differences between mean PWP and approximately the same CWP. The increased mean PWP in turbulent *N*60 and *N*30 cases represent effects of turbulence on drizzle/rain formation. Enhanced drizzle/rain imply more efficient removal of cloud water as illustrated by the differences in low and high CCN simulations in Fig. 9. It follows that the only explanation why the CWP remains approximately the same in corresponding turbulent and gravitational simulations (around 11.2 and 7.1 $\mathrm{g\,m^{-2}}$ in *N*60 and *N*30, respectively) is the dynamic enhancement, that is, slightly deeper on average clouds in simulations considering turbulent kernel. This aspect is not obvious in Fig. 9 and will be subject of a future investigation.

Figures 13 and 14 show evolutions of the cumulative rainfall at the cloud base and at the surface (i.e. integrated over time mean rain rate at these heights) in simulations *N*30, *N*60, and *N*120 applying linear and logarithmic scales, respectively. We consider both the cloud base and the surface to document effects of rain evaporation between the cloud layer and the surface, but this aspect is only marginally relevant as shown by the figures. The key point is that regardless whether the cloud base or the surface is considered, the turbulent enhancement of droplet collisions has a dramatic impact, with rain accumulations after 6 h several times larger than applying the gravitational kernel.

ACPD
13, 9217–9265, 2013

Such an effect qualitatively agrees with the impacts reported in Seifert et al. (2010, see Table II in particular).

6 Summary and conclusions

This paper discusses LES simulations of a field of shallow convective clouds aiming at quantitative assessment of the impact of cloud turbulence on warm rain processes. The study provides a climax of around a decade long collaborative research between the University of Delaware and NCAR that resulted in the development of cloud droplet collection kernels that include effects of cloud turbulence. These kernels were developed through theoretical studies guided by DNS and more recently HDNS simulations. Effects of turbulence on rain formation is a difficult multiscale problem, concerning processes taking place over a wide range of spatial scales. Formation and growth of cloud droplets (by water vapor diffusion and collision-coalescence) takes place at scales from submicron to tens and hundreds of microns. Small-scale cloud dynamics concerns scales within the inertial range of atmospheric turbulence, from scales at which cloud TKE is generated (tens to hundreds of meters) down to the Kolmogorov microscale, around a millimeter in typical atmospheric conditions. Larger-scale cloud and precipitation dynamics involves such processes as cloud initiation, formation of cloud updrafts and downdrafts, interactions between precipitation-laden downdrafts and the surface, etc. It involves spatial scales of hundred of meters to a few kilometers. Finally, at even larger scales, mesoscale processes determine overall characteristics of a field of precipitating clouds (cloud depth, cloud cover, etc). The range, from submicron to tens of kilometers, represents about 10 decades of spatial scales, and it will never be fully resolved in numerical simulations. However, with the availability of the petascale computing resources, we aim at extending our collaborative research towards reducing the scale gap between top-down LES of cloud dynamics (bin EULAG) and a bottom-up HDNS of cloud microphysics. Ultimately, both approaches may result in the near future in an integrated multiscale (in time and space) simulation environment which truly

ACPD
13, 9217–9265, 2013

overlap at the $O(1\,\mathrm{m})$ spatial scales. This effort will offer an opportunity to develop new parameterizations of various cloud physical processes unresolved in weather and climate models.

We applied previously-developed collection kernels that include effects of cloud turbulence to LES cloud-scale simulations using bin microphysics and targeted shallow convective clouds where turbulence effects are expected to be significant. Except for applying the bin microphysics, our study follows Seifert et al. (2010) where the simulation setup based on the RICO (Rain In Cumulus over Ocean) model intercomparison case was used (van Zanten et al., 2010). We apply the BOMEX case (Siebesma et al., 2003) because it approximately maintains the initial atmospheric state in the non-precipitating case, and it was used in our previous studies (e.g. Slawinska et al., 2012; Wyszogrodzki et al., 2011).

Before applying the turbulent kernel in LES simulations, we first addressed the role of the flow intermittency, an aspect not considered in previous studies. This is a relevant issue and its importance can be justified in the following way. The turbulent enhancement of the gravitational kernel depends nonlinearly on the turbulence characteristics, and these characteristics strongly fluctuate in time and space due to the flow intermittency. Because of computational limitations, the LES gridbox is typically much larger than the computational domain applied in the DNS and HDNS studies. It follows that the mean dissipation rate predicted by LES may represent rate of droplet collisions that is different from the rate that considers spatial variability of the dissipation rate. We investigated this problem by comparing the turbulent kernel derived applying the mean dissipation rate with the averaged kernel applying the distribution of the dissipation rates following the Kolmogorov (1962) refined similarity theory. The analysis showed, perhaps to some surprise, that the effects become significant (the relative difference above 10 %) only for high dissipation rates (above 100 $\mathrm{cm}^2\,\mathrm{s}^{-3}$) and large (higher than 10) ratios between LES gridlength and DNS domain size. As a result, and considering still uncertain formulation of the turbulent kernel, we decided to exclude these effects from our analysis. Consequently, we simply apply the turbulence-enhanced collection

ACPD
13, 9217–9265, 2013

kernels based on the local TKE predicted by the LES model and excluding effects of the subgrid-scale variability of TKE dissipation (i.e. applying the same methodology as in Seifert et al., 2010). Note that this issue becomes less problematic once the LES gridlength approaches the size of the computational domain applied in DNS and HDNS studies.

To highlight physical processes responsible for the impact of cloud turbulence on the rain development, we presented simple 2-D simulations of a precipitating thermal. These simulations show that rain develops earlier and more rain falls from the thermal when turbulent effects are included. The former effect was anticipated based on our previous idealized studies and it comes from faster completion of the autoconversion phase of rain formation. The latter effect comes from a combination of two different mechanisms. Firstly, if drizzle forms earlier, then more cloud water is available to be converted into precipitation throughout the cloud lifecycle. We refer to this as the microphysical enhancement. Secondly, when rain develops and falls out from a cloudy volume, then the buoyancy of the volume is increased and the volume can rise higher and produce more cloud water to be converted into precipitation. This feedback from the cloud microphysics into cloud dynamics can be referred to as the dynamical enhancement. In idealized rising thermal simulations, the microphysical and dynamical enhancement contribute about equally to the overall effect, with simulations including turbulent effects resulting in about a twofold increase of the surface rainfall. However, these simulations need to be treated with much caution because of their significant simplifications.

Cloud field simulations also show a combination of microphysical and dynamical enhancements, although quantification of their relative contribution is difficult. Because the primary factor affecting ability of a cloud to precipitate is the concentration of cloud droplets (which determines the maximum size of diffusionally-grown droplets given the cloud depth), we performed simulations with a range of prescribed CCN concentrations (30, 60, 120, and 240 mg^{-1}). Only small amounts of drizzle/rain were simulated within clouds for the highest CCN concentration, and the turbulent kernel led to increased

ACPD
13, 9217–9265, 2013

amounts of drizzle/rain. Rain below the cloud base was not present in gravitational or turbulent kernel simulations. For the CCN concentration of 120 mg^{-1}, rain occasionally reached the surface in the turbulent kernel simulation, but not when applying the gravitational kernel. In simulations using 30 and 60 mg^{-1} CCN concentrations, rain reached the surface regardless of the type of kernel used. However, the 6 h accumulations were significantly larger when using the turbulent kernel. The accumulations were around 13 and 1 mm for the gravitational kernel assuming 30 and 60 mg^{-1} CCN concentration, respectively, and around 50 and 12 mm for corresponding simulations applying turbulent kernel. These imply a dramatic increase when effects of cloud turbulence are included, in line with the enhancement presented in Seifert et al. (2010, see Table II therein). The dynamical enhancement resulted in time-averaged CWPs similar between gravitational and turbulent kernel simulations, despite significant differences in PWP and rainfall. Simulations with small or no rainfall below the cloud base showed only effects of the microphysical enhancement.

Simulations reported in this paper have to be considered as just an initial step in the quantification of turbulent effects on warm-rain processes. As shown in Seifert et al. (2010), higher spatial resolution in LES simulations not only leads to a significantly different surface rain rate, but also to a different enhancement factor (see Table II therein). This suggests that higher spatial resolution bin simulations of the type reported here should be considered in the future. Work should also continue to obtain and use improved formulations of the turbulent kernel and include effects of small-scale turbulence intermittency in LES simulations. Applying different formulation of the cloud microphysics (e.g. based on the Lagrangian approach, Andrejczuk et al., 2010) should also be used to ensure that limitations of the bin microphysics approach do not play any significant role. Finally, since simulated effects of cloud turbulence are dramatic, one should attempt to use remote sensing observations (either ground-based or from space) in an attempt to validate the impacts. All these aspects warrant future investigations and we hope to report on some of them in forthcoming publications.

ACPD
13, 9217–9265, 2013

Appendix A

The turbulent collection kernel

In this appendix, we summarize the formulation used to specify the turbulent collection kernel K_{ij}. All necessary details and relationships are compiled together here so the parameterization can be readily implemented by others to include effects of air turbulence when modeling droplet growth by collision-coalescence. The kernel combines the theoretical turbulent geometric collection kernel K_{ij}^{tg}, gravitational collision efficiency E_{ij}^{g}, and collision-efficiency enhancement factor η_E as

$$K_{ij} = K_{ij}^{tg} \times E_{ij}^{g} \times \eta_E. \tag{A1}$$

The gravitational collision efficiency E_{ij}^{g} is obtained by interpolation from tabulated data in Hall (1980). The collision-effciency enhancement factor η_E is interpolated from the hybrid DNS data in Wang et al. (2005).

The formulation for K_{ij}^{tg} follows Ayala et al. (2008b), which states

$$K_{ij}^{tg} = 2\pi R^2 \langle |w_r| \rangle g_{ij},$$

where $R = a_i + a_j$, the sum of the radii of two colliding droplets.

The average radial relative velocity $\langle |w_r| \rangle$ is computed by

$$\langle |w_r| \rangle = \sqrt{\frac{2}{\pi}} \sigma f(b)$$

$$f(b) = \frac{1}{2}\sqrt{\pi}\left(b + \frac{0.5}{b}\right)\mathrm{erf}(b) + \frac{1}{2}\exp(-b^2)$$

$$b = \frac{|\mathbf{g}| \times |\tau_{p_i} - \tau_{p_j}|}{\sigma\sqrt{2}}$$

ACPD
13, 9217–9265, 2013

or alternatively by the following approximation, with less than 2.5 % relative error, as

$$\langle |w_r| \rangle = \sqrt{\frac{2}{\pi}} \left(\sigma + \frac{\pi}{8} (\tau_{p_i} - \tau_{p_j})^2 |\mathbf{g}|^2 \right)^{1/2},$$

where $\sigma^2 = < (v'^{(i)})^2 > + < (v'^{(j)})^2 > - 2 < (v'^{(i)} v'^{(j)}) >$, and

$$< (v'^{(k)})^2 > = \frac{u'^2}{\tau_{p_k}} [b_1 d_1 \Psi(c_1, e_1) - b_1 d_2 \Psi(c_1, e_2) - b_2 d_1 \Psi(c_2, e_1) + b_2 d_2 \Psi(c_2, e_2)],$$

$$< (v'^{(i)} v'^{(j)}) > = \frac{u'^2 f_2(R)}{\tau_{p_i} \tau_{p_j}} [b_1 d_1 \Phi(c_1, e_1) - b_1 d_2 \Phi(c_1, e_2) - b_2 d_1 \Phi(c_2, e_1) + b_2 d_2 \Phi(c_2, e_2)],$$

where the longitudinal two-point velocity correlation evaluated at $r = R$ is

$$f_2(R) = \frac{1}{2(1 - 2\beta^2)^{1/2}} \left\{ \left(1 + \sqrt{1 - 2\beta^2} \right) \times \exp \left[- \frac{2R}{\left(1 + \sqrt{1 - 2\beta^2} \right) L_e} \right] - \left(1 - \sqrt{1 - 2\beta^2} \right) \times \exp \left[- \frac{2R}{\left(1 - \sqrt{1 - 2\beta^2} \right) L_e} \right] \right\}.$$

ACPD
13, 9217–9265, 2013

The constants b_1, b_2, c_1, c_2, d_1, d_2, e_1, and e_2 are defined as

$$b_1 = \frac{1+\sqrt{1-2z^2}}{2\sqrt{1-2z^2}}, \qquad b_2 = \frac{1-\sqrt{1-2z^2}}{2\sqrt{1-2z^2}},$$

$$c_1 = \frac{(1+\sqrt{1-2z^2})T_L}{2}, \qquad c_2 = \frac{(1-\sqrt{1-2z^2})T_L}{2},$$

$$d_1 = \frac{1+\sqrt{1-2\beta^2}}{2\sqrt{1-2\beta^2}}, \qquad d_2 = \frac{1-\sqrt{1-2\beta^2}}{2\sqrt{1-2\beta^2}},$$

$$e_1 = \frac{(1+\sqrt{1-2\beta^2})L_e}{2}, \qquad e_2 = \frac{(1-\sqrt{1-2\beta^2})L_e}{2},$$

where $z = \tau_T/T_L$, and $\beta = \sqrt{2}\lambda/L_e$.

The function $\Phi(\alpha,\phi)$, taking $v_{p_i} > v_{p_j}$, is given by

$$\Phi(\alpha,\phi) = \left\{\frac{1}{Aj_1} - \frac{1}{Ai_1}\right\} \times \frac{v_{p_i} - v_{p_j}}{2\phi\left(\frac{v_{p_i}-v_{p_j}}{\phi} + \frac{1}{\tau_{p_i}} + \frac{1}{\tau_{p_j}}\right)^2}$$

$$+ \left\{\frac{4}{Aj_3} - \frac{1}{(Aj_2)^2} - \frac{1}{(Aj_1)^2}\right\} \times \frac{v_{p_j}}{2\phi\left[\frac{1}{\tau_{p_i}} - \frac{1}{\alpha} + \left(\frac{1}{\tau_{p_j}} + \frac{1}{\alpha}\right)\frac{v_{p_i}}{v_{p_j}}\right]}$$

$$+ \left\{\frac{2\phi}{Ai_1} - \frac{2\phi}{Aj_1} - \frac{v_{p_i}}{(Ai_1)^2} + \frac{v_{p_j}}{(Aj_1)^2}\right\} \times \frac{1}{2\phi\left(\frac{v_{p_i}-v_{p_j}}{\phi} + \frac{1}{\tau_{p_i}} + \frac{1}{\tau_{p_j}}\right)}$$

ACPD
13, 9217–9265, 2013

where

$$Ai_1 = \frac{v_{p_i}}{\phi} + \frac{1}{\tau_{p_i}} + \frac{1}{\alpha} \qquad Aj_1 = \frac{v_{p_j}}{\phi} - \frac{1}{\tau_{p_j}} - \frac{1}{\alpha}$$

$$Aj_2 = \frac{v_{p_j}}{\phi} + \frac{1}{\tau_{p_j}} + \frac{1}{\alpha} \qquad Aj_3 = \left(\frac{v_{p_j}}{\phi}\right)^2 - \left(\frac{1}{\tau_{p_j}} + \frac{1}{\alpha}\right)^2$$

and $\Psi(\alpha,\phi)$, for k either i or j is

$$\Psi(\alpha,\phi) = \frac{1}{\frac{1}{\tau_{p_k}} + \frac{1}{\alpha} + \frac{v_{p_k}}{\phi}} - \frac{v_{p_k}}{2\phi\left(\frac{1}{\tau_{p_k}} + \frac{1}{\alpha} + \frac{v_{p_k}}{\phi}\right)^2}$$

The radial distribution function at contact g_{ij} is given by

$$g_{ij} = \left(\frac{\eta^2 + {r_c}^2}{R^2 + {r_c}^2}\right)^{C_1/2}, \text{with} C_1 = \frac{y(St)}{\left(|\mathbf{g}|/(v_k/\tau_k)\right)^{f_3(R_\lambda)}},$$

where

$$y(St) = -0.1988St^4 + 1.5275St^3 - 4.2942St^2 + 5.3406St,$$

$$f_3(R_\lambda) = 0.1886 \exp\left(\frac{20.306}{R_\lambda}\right),$$

and $St \equiv \max(St_j, St_i)$. Since the fitting for $y(St)$ was done for a limited range of St in DNS, it should be set to zero for large St when the function $y(St)$ becomes negative.

The expression for r_c is written as

$$\left(\frac{r_c}{\eta}\right)^2 = |St_j - St_i| F(a_{o_g}, R_\lambda)$$

ACPD
13, 9217–9265, 2013

where a_{o_g} is

$$a_{o_g} = a_o + \frac{\pi}{8}\left(\frac{|\mathbf{g}|}{\nu_K/\tau_K}\right)^2$$

and $F(a_{o_g}, R_\lambda)$

$$F(a_{o_g}, R_\lambda) = 20.115\left(\frac{a_{o_g}}{R_\lambda}\right)^{1/2}.$$

In the above parameterization, the input parameters are: (1) for the droplets, the radii a_i and a_j, and the water density ρ_w; (2) for the turbulent air flow, the density ρ, the viscosity ν, the turbulence dissipation rate ϵ, and the Taylor-microscale Reynolds number R_λ, and (3) the gravitational acceleration $|\mathbf{g}|$. If R_λ is not known, we estimate the rms fluctuation velocity u' by $u' = 202.0\,(\epsilon/400.0)^{1/3}$, with u' in cm/s and the dissipation rate ϵ in $\mathrm{cm}^2\,\mathrm{s}^{-3}$ (Wang et al., 2006a). All other derived variables used in the model are listed in Table 2.

Acknowledgements. This work was supported by the NSF through grants OCI-0904534 and OCI-0904449. AAW was also supported by NSF grant OCI-0904599. WWG was partially supported by the NSF Science and Technology Center for Multiscale Modeling of Atmospheric Processes (CMMAP; managed by Colorado State University under cooperative agreement ATM-0425247) and by the DOE ASR grant DE-SC0008648. LPW also acknowledges visitor support from the NCAR's Geophysical Turbulence Program (GTP). Computer time at NCAR was provided by NSF through MRI grants CNS-0421498, CNS-0420873, CNS-0420985, NSF sponsorship of the National Center for Atmospheric Research, the University of Colorado, and a grant from the IBM Shared University Research (SUR) program. National Center for Atmospheric Research is sponsored by the National Science Foundation.

ACPD
13, 9217–9265, 2013

References

Ayala, O., Grabowski, W. W., and Wang, L- P.: A hybrid approach for simulating turbulent collisions of hydrodynamically-interacting particles, J. Comput. Phys., 225, 51–73, 2007.

Ayala, O., Rosa, B., Wang, L- P., and Grabowski, W. W.: Effects of turbulence on the geometric collision rate of sedimenting droplets: Part 1: Results from direct numerical simulation, New J. Phys., 10, 075015, doi:10.1088/1367-2630/10/7/075015, 2008a.

Ayala, O., Rosa, B., and Wang, L- P.: Effects of turbulence on the geometric collision rate of sedimenting droplets: Part 2: Theory and parameterization, New J. Phys., 10, 075016, also Corrigendum, New J. Phys., 10, 099802, doi:10.1088/1367-2630/10/7/075016, 2008b.

Beard, K. V.: Terminal velocity and shape of cloud and precipitation drops aloft, J. Atmos. Sci., 33, 851–864, 1976.

Bott, A.: A positive definite advection scheme obtained by nonlinear renormalization of the advective fluxes, Mon. Weather Rev., 117, 1006–1015, 1998.

Chun, J., Koch, D. L., Rani, S. L., Ahluwalia, A., and Collins, L. R.: Clustering of aerosol particles in isotropic turbulence, J. Fluid Mech., 536, 219–251, 2005.

Dávila, J. and Hunt, J. C. R.: Settling of small particles near vortices and in turbulence, J. Fluid Mech., 440, 117–145, 2001.

Franklin, C. N., Vaillancourt, P. A., Yau, M. K., and Bartello, P.: Collision rates of cloud droplets in turbulent flow, J. Atmos. Sci., 62, 2451–2466, 2005.

Grabowski, W. W.: Indirect impact of atmospheric aerosols in idealized simulations of convective-radiative quasi-equilibrium, J. Climate, 19, 4664–4682, 2006.

Grabowski, W. W.: Representation of turbulent mixing and buoyancy reversal in bulk cloud models, J. Atmos. Sci., 64, 3666–3690, 2007.

Grabowski, W. W. and Wang, L.-P.: Diffusional and accretional growth of water drops in a rising adiabatic parcel: effects of the turbulent collision kernel, Atmos. Chem. Phys., 9, 2335–2353, doi:10.5194/acp-9-2335-2009, 2009.

Grabowski, W. W. and Wang, L.-P.: Growth of cloud droplets in a turbulent environment, Annu. Rev. Fluid Mech., 45, 293–324, 2013.

Grabowski, W. W., Thouron, O., Pinty, J.-P., and Brenguier, J.-L.: A hybrid bulk-bin approach to model warm-rain processes, J. Atmos. Sci., 67, 385–399, 2010.

Grabowski, W. W., Andrejczuk, M., and Wang, L.-P.: Droplet growth in a bin warm-rain scheme with Twomey CCN activation, Atmos. Res., 99, 290–301, 2011.

ACPD
13, 9217–9265, 2013

Hall, W. D.: A detailed microphysical model within a two-dimensional framework: model description and preliminary results, J. Atmos. Sci., 37, 2486–2507, 1980.
Holland, J. Z. and Rasmusson, E. M.: Measurements of the atmospheric mass, energy, and momentum budgets over a 500 kilometer square of tropical ocean, Mon. Weather Rev., 101, 44–55, 1973.
Jarecka, D., Grabowski, W. W., and Pawlowska, H.: Modeling of subgrid-scale mixing in large-eddy simulation of shallow convection, J. Atmos. Sci., 66, 2125–2133, 2009.
Jarecka, D., Grabowski, W. W., Pawlowska, H., and Wyszogrodzki, A. A.: Modeling of subgrid-scale cloud-clear air turbulent mixing in large eddy simulation of cloud fields, J. Phys. Conf. Ser., 318, 072010, doi:10.1088/1742-6596/318/7/072010, 2011.
Khain, A., Ovtchinnikov, M., Pinsky, M., Pokrovsky, A., and Krugliak, H.: Notes on the state-of-the-art numerical modeling of cloud microphysics, Atmos. Res., 55, 159–224, 2000.
Kogan, Y. L.: The simulation of a convective cloud in a 3-D model with explicit microphysics. Part I: Model description and sensitivity experiments, J. Atmos. Sci., 48, 1160–1189, 1991.
Kolmogorov, A. N.: A refinement of previous hypotheses concerning the local structure of turbulence in a viscous incompressible fluid at high Reynolds number, J. Fluid Mech., 13, 82–85, 1962.
Margolin, L. G., Smolarkiewicz, P. K., and Sorbjan, Z.: Large-eddy simulations of convective boundary layers using nonoscillatory differencing, Physica D, 133, 390–397, 1999.
Pinsky, M. B. and Khain, A. P.: Collisions of small drops in a turbulent flow. Part II: Effects of flow accelerations, J. Atmos. Sci., 61, 1926–1939, 2004.
Pinsky, M. B., Khain, A. P., and Shapiro, M.: Collisions of small drops in a turbulent flow. Part I: Collision efficiency. Problem formulation and preliminary results, J. Atmos. Sci., 56, 2585–2600, 1999.
Pope, S. B.: Turbulent Flows, Cambridge University Press, Cambridge, UK, 771 pp., 2000.
Pruppacher, H. R. and Klett, J. D.: Microphysics of Clouds and Precipitation, Kluwer Academic, 954 pp., Kluwer Academic, Dordrecht, the Netherlands, 1997.
Prusa, J. M., Smolarkiewicz, P. K., and Wyszogrodzki, A. A.: EULAG, a computational model for multiscale flows, Comput. Fluids, 37, 1193–1207, 2008.
Rosa, B., Parishani, H., Ayala, O., Wang, L.-P., and Grabowski, W. W.: Kinematic and dynamic pair collision statistics of sedimenting inertial particles relevant to warm rain initiation, J. Phys. Conf. Ser., 318, 072016, doi:10.1088/1742-6596/318/7/072016, 2011.

ACPD
13, 9217–9265, 2013

Rosa, B., Parishani, H., Ayala, O., Wang, L.-P., and Grabowski, W. W.: Kinematic and dynamic collision statistics of cloud droplets from high-resolution simulations, New J. Phys., accepted, 2013.

Seifert, A., Nuijens, L., and Stevens, B.: Turbulence effects on warm-rain autoconversion in precipitating shallow convections, Q. J. Roy. Meteor. Soc., 136, 1753–1762, doi:10.1002/qj.684, 2010.

Schumann, U.: Subgrid length-scales for large-eddy simulation of stratified turbulence, Theor. Comp. Fluid Dyn., 2, 279–290, 1991.

Siebesma, A. P., Bretherton, C. S., Brown, A., Chlond, A., Cuxart, J., Duynkerke, P. G., Jiang, H., Khairoutdinov, M., Lewellen, D., Moeng, C.-H., Sanchez, E., Stevens, B., and Stevens, D. E.: A large eddy simulation intercomparison study of shallow cumulus convection, J. Atmos. Sci., 60, 1201–1219, 2003.

Slawinska, J., Grabowski, W. W., Pawlowska, H., and Morrison, H.: Droplet activation and mixing in large-eddy simulation of a shallow cumulus field, J. Atmos. Sci., 69, 444–462, 2012.

Sreenivasan, K. R. and Antonia, R. A.: The Phenomenology of small-scale turbulence, Annu. Rev. Fluid Mech., 29, 435–472, 1997.

Sreenivasan, K. R. and Kailasnath, P.: An update on the intermittency exponent in turbulence, Phys. Fluids A-Fluid, 5, 512–514, 1993.

Van Zanten, M. C., Stevens, B. B., Nuijens, L., Siebesma, A. P., Ackerman, A., Burnet, F., Cheng, A., Couvreux, F., Jiang, H., Khairoutdinov, M., Kogan, Y., Lewellen, D. C., Mechem, D., Nakamura, K., Noda, A., Shipway, B. J., Slawinska, J., Wang, S., and Wyszogrodzki, A.: Controls on precipitation and cloudiness in simulations of trade-wind cumulus as observed during RICO, J. Adv. Model. Earth Syst., 3, M06001, doi:10.1029/2011MS000056, 2010.

Wang, L.-P. and Maxey, M. R.: Settling velocity and concentration distribution of heavy particles in homogeneous isotropic turbulence, J. Fluid Mech., 256, 27–68, 1993.

Wang, L.-P., Ayala, O., Kasprzak, S. E., and Grabowski, W. W.: Theoretical formulation of collision rate and collision efficiency of hydrodynamically-interacting cloud droplets in turbulent atmosphere, J. Atmos. Sci., 62, 2433–2450, 2005.

Wang, L.-P., Ayala, O., Xue, Y., and Grabowski, W. W.: Comments on “Droplets to drops by turbulent coagulation”, J. Atmos. Sci., 63, 2397–2401, 2006a.

ACPD
13, 9217–9265, 2013

Wang, L.-P., Franklin, C. N., Ayala, O., and Grabowski, W. W.: Probability distributions of angle of approach and relative velocity for colliding droplets in a turbulent flow, J. Atmos. Sci., 63, 881–900, 2006b.

Wang, L.-P., Ayala, O., Rosa, B., and Grabowski, W. W.: Turbulent collision efficiency of heavy particles relevant to cloud droplets, New J. Phys., 10, 075013, doi:10.1088/1367-2630/10/7/075013, 2008.

Wyszogrodzki, A. A., Grabowski, W. W., and Wang, L.-P.: Activation of cloud droplets in bin-microphysics simulation of shallow convection, Acta Geophys., 59, 1168–1183, doi:10.2478/s11600-011-0052-y, 2011.

Xue, Y., Wang, L.-P., and Grabowski, W. W.: Growth of cloud droplets by turbulent collision-coalescence, J. Atmos. Sci., 65, 331–356, 2008.

Zaichik, L. I. and Alipchenkov, V. M.: Pair dispersion and preferential concentration of particles in isotropic turbulence, Phys. Fluids, 15, 1776–1787, 2003.

Zaichik, L. I., Simonin, O., and Alipchenkov, V. M.: Two statistical models for predicting collision rates of inertial particles in homogeneous isotropic turbulence, Phys. Fluids, 15, 2995–3005, 2003.

Zhou, Y., Wexler, A. S., and Wang, L.-P.: Modeling turbulent collision of bidisperse inertial particles, J. Fluid Mech., 433, 77–104, 2001.

ACPD
13, 9217–9265, 2013

Table 1. The enhancement factor η_E of the collision efficiency. The upper/lower part of the table is for $\epsilon = 100/400\,\mathrm{cm^2\,s^{-3}}$.

a_2/a_1	$a_1 = 10\,\mu m$	$20\,\mu m$	$30\,\mu m$	$40\,\mu m$	$50\,\mu m$	$60\,\mu m$	$100\,\mu m$
$\rightarrow$ 0.0	1.74	1.74	1.773	1.49	1.207	1.207	1.0
0.1	1.46	1.46	1.421	1.245	1.069	1.069	1.0
0.2	1.32	1.32	1.245	1.123	1.000	1.000	1.0
0.3	1.250	1.250	1.148	1.087	1.025	1.025	1.0
0.4	1.186	1.186	1.066	1.060	1.056	1.056	1.0
0.5	1.045	1.045	1.000	1.014	1.028	1.028	1.0
0.6	1.070	1.070	1.030	1.038	1.046	1.046	1.0
0.7	1.000	1.000	1.054	1.042	1.029	1.029	1.0
0.8	1.223	1.223	1.117	1.069	1.021	1.021	1.0
0.9	1.570	1.570	1.244	1.166	1.088	1.088	1.0
1.0	20.3	20.3	14.6	8.61	2.60	2.60	1.0
$\rightarrow$ 0.0	4.976	4.976	3.593	2.519	1.445	1.445	1.0
0.1	2.984	2.984	2.181	1.691	1.201	1.201	1.0
0.2	1.988	1.988	1.475	1.313	1.150	1.150	1.0
0.3	1.490	1.490	1.187	1.156	1.126	1.126	1.0
0.4	1.249	1.249	1.088	1.090	1.092	1.092	1.0
0.5	1.139	1.139	1.130	1.091	1.051	1.051	1.0
0.6	1.220	1.220	1.190	1.138	1.086	1.086	1.0
0.7	1.325	1.325	1.267	1.165	1.063	1.063	1.0
0.8	1.716	1.716	1.345	1.223	1.100	1.100	1.0
0.9	3.788	3.788	1.501	1.311	1.120	1.120	1.0
1.0	36.52	36.52	19.16	22.80	26.0	26.0	1.0

ACPD
13, 9217–9265, 2013

Table 2. List of derived variables used in the parameterization.

Flow variable	Definition
Kolmogorov time	$\tau_K = \left(\frac{\nu}{\epsilon}\right)^{1/2}$
Kolmogorov length	$\eta = \left(\frac{\nu^3}{\epsilon}\right)^{1/4}$
Kolmogorov velocity	$v_K = (\nu\epsilon)^{1/4}$
Rms component fluctuation velocity	$u' = \frac{R_\lambda^{1/2}}{15^{1/4}} v_K$
Lagrangian integral time	$T_L = \frac{u'^2}{\epsilon}$
Large-eddy turnover time	$L_e = 0.5\frac{u'^3}{\epsilon}$
Lagrangian Taylor microscale time	$\tau_T = \left(\frac{2R_\lambda}{15^{1/2}a_o}\right)^{1/2} \tau_K$
Scale of acceleration variance	$a_o = \frac{11+7R_\lambda}{205+R_\lambda}$
Taylor microscale	$\lambda = u'\left(\frac{15\nu}{\epsilon}\right)^{1/2}$
Droplet variable	**Definition**
Inertial response time	$\tau_p = \frac{2}{9}\frac{\rho_w}{\rho}\frac{a^2}{\nu f(Re_p)}$
Nonlinear drag factor	$f(Re_p) = 1 + 0.15Re_p^{0.687}$
Still-fluid Stokes terminal velocity	$v_p = \tau_p\lvert\mathbf{g}\rvert$
Droplet Reynolds number	$Re_p = \frac{2av_p}{\nu}$
Stokes number	$St = \frac{\tau_p}{\tau_K}$

ACPD
13, 9217–9265, 2013

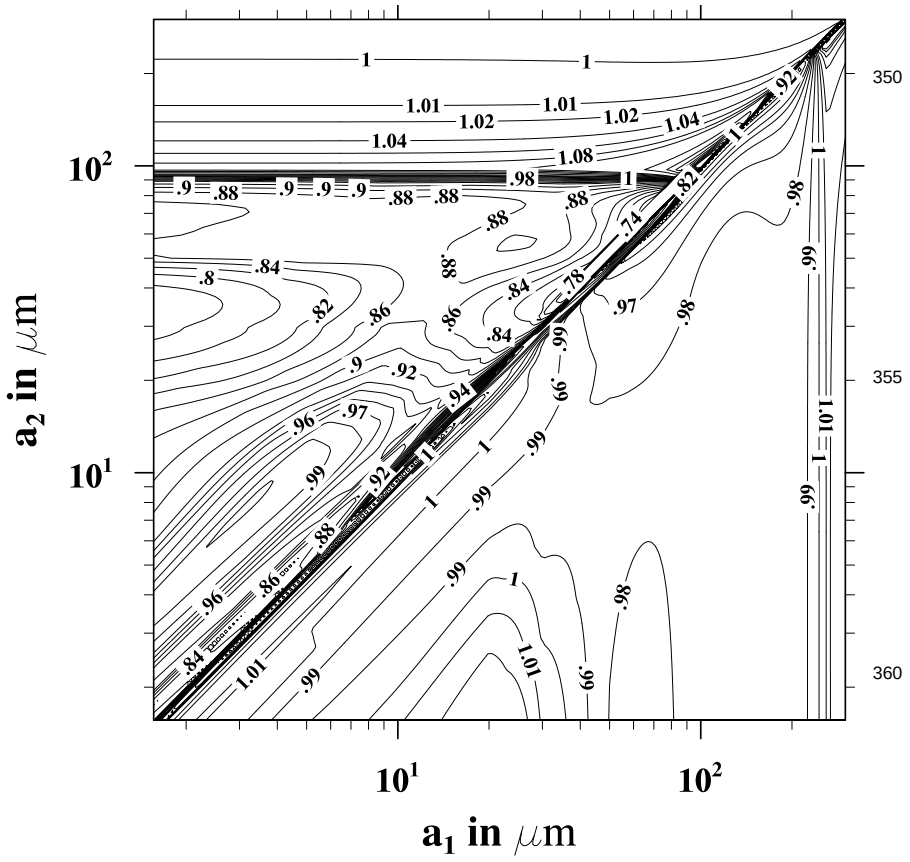

Fig. 1. Contour lines of the ratio $\mathcal{R}$ for $\epsilon_2 = 50\,\mathrm{cm^2\,s^{-3}}$ (lower right) and $\epsilon_2 = 500\,\mathrm{cm^2\,s^{-3}}$ (upper left), with $l_2/l_1 = 50$ and $l_1 = 0.5\,\mathrm{m}$. Since $\mathcal{R}(a_1, a_2) = \mathcal{R}(a_2, a_1)$, therefore, only half of the domain is shown for each ϵ_2.

ACPD
13, 9217–9265, 2013

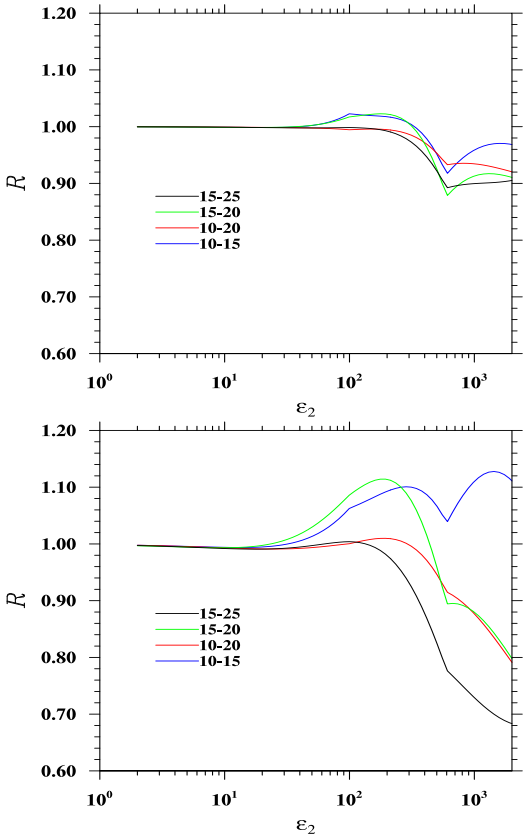

Fig. 2. The ratio $\mathcal{R}$ as a function of the dissipation rate ϵ_2 (in $\mathrm{cm}^2\,\mathrm{s}^{-3}$) for selected pairs of droplet radii (in μm) and for $l_2/l_1 = 10$ (upper panel) and $l_2/l_1 = 1000$ (lower panel).

ACPD
13, 9217–9265, 2013

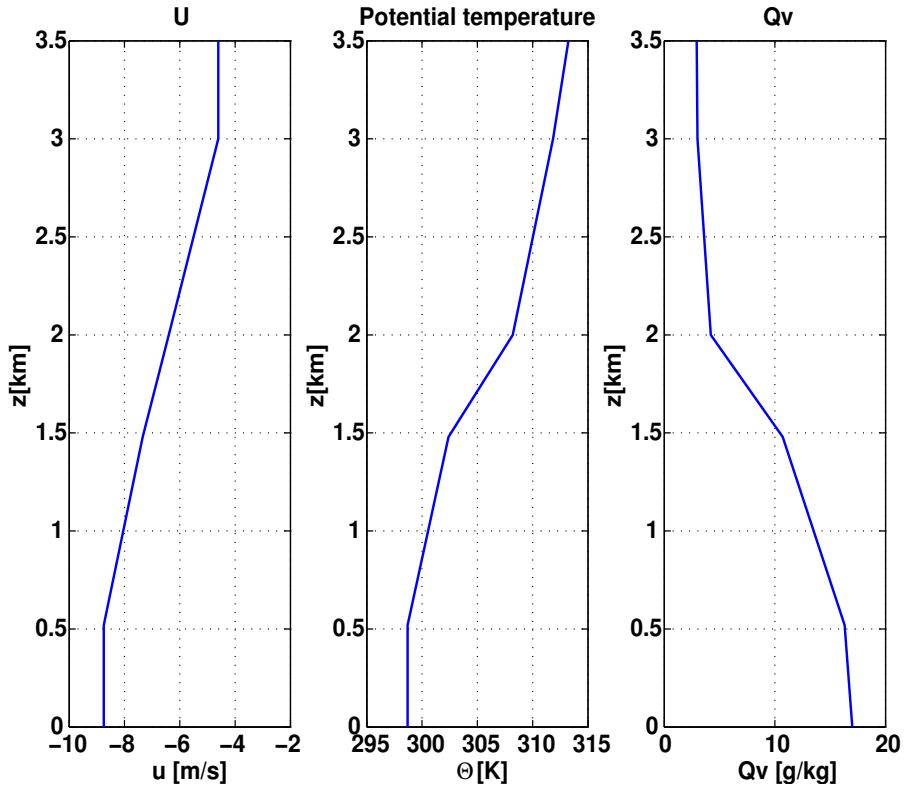

Fig. 3. Initial environmental profiles.

ACPD
13, 9217–9265, 2013

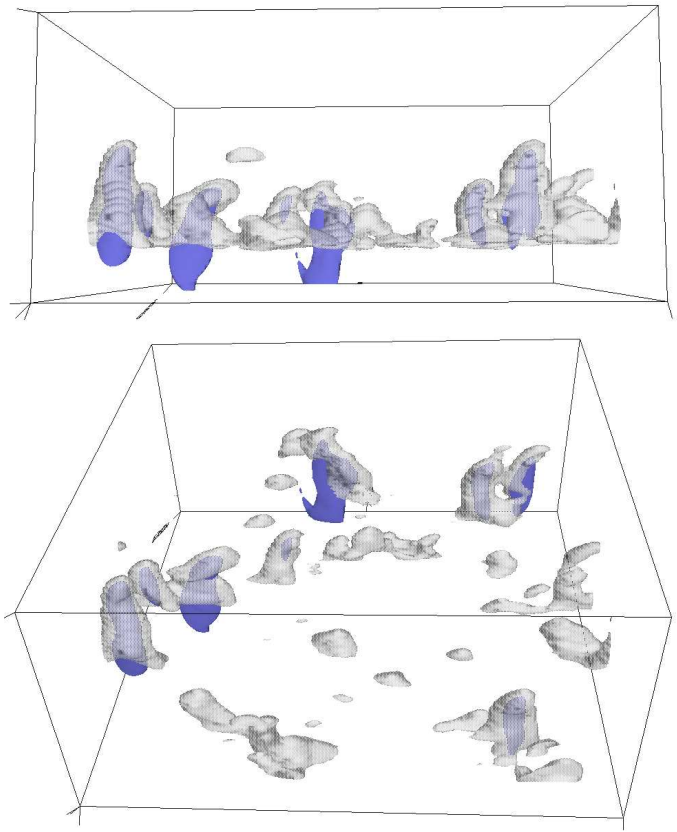

Fig. 4. Snapshots of cloud water mixing ratio q_c (transparent gray) and rain water mixing ratio q_r (solid blue) at the 6th hour of the simulation. The isosurfaces show values $q_c = 0.05\,\mathrm{g\,kg^{-1}}$ and $q_r = 0.02\,\mathrm{g\,kg^{-1}}$.

ACPD
13, 9217–9265, 2013

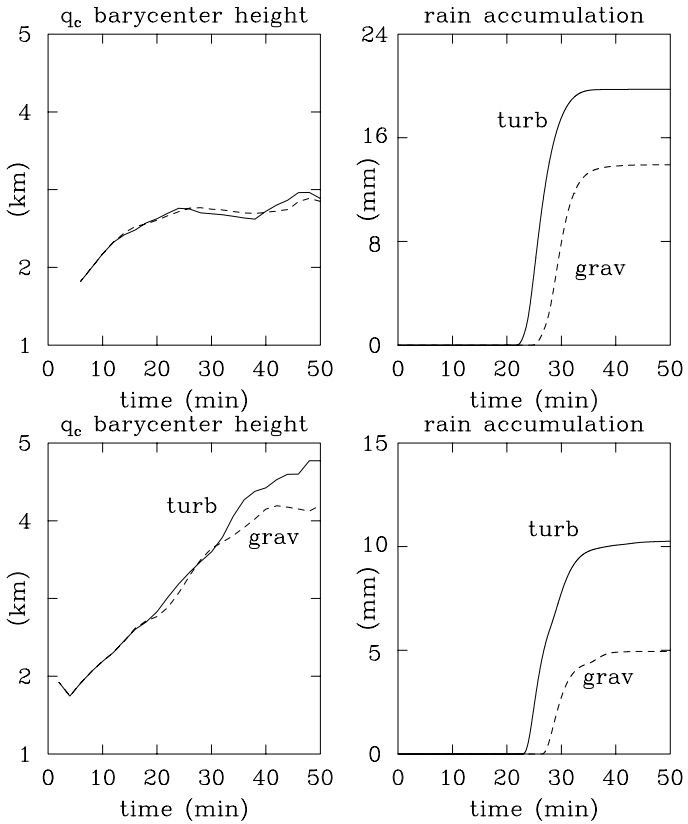

Fig. 5. The evolution of the height of the cloud water center of mass (left panels) and the surface total rain accumulation (right panels) for 2-D rising thermal simulations. Upper panels come from simulations where the thermal rise is arrested in the middle of the domain by the layer of increased stability. Lower panels show results from simulations where the thermal can rise unobstructed towards the upper model boundary.

ACPD
13, 9217–9265, 2013

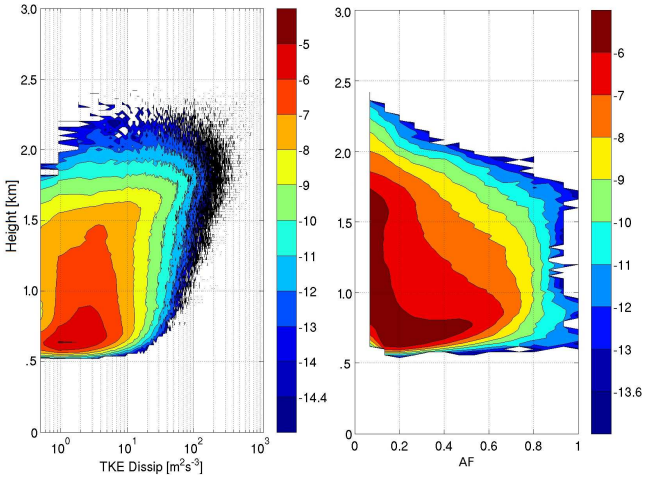

Fig. 6. The contoured frequency by altitude diagrams (CFADs) of the dissipation rate (in $cm^2 s^{-3}$) and adiabatic fraction AF inside volumes with cloud water mixing ratio $q_c > 0.01\,kg\,kg^{-1}$. The logarithm of the frequency (with respect to the number of cloudy points at a given height) is shown on the colorbars.

ACPD
13, 9217–9265, 2013

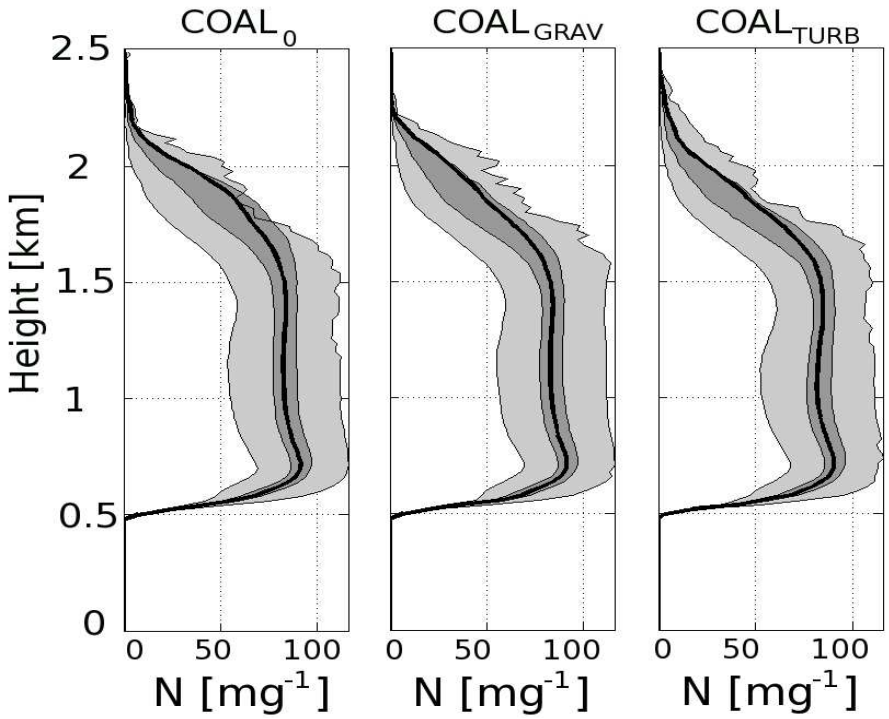

Fig. 7. Percentiles of the total drop concentration for the *N*120 case. Left, middle, and right panels show results from simulations without collision-coalescence, with gravitational collision-coalescence, and with turbulence-enhanced collision-coalescence, respectively.

ACPD
13, 9217–9265, 2013

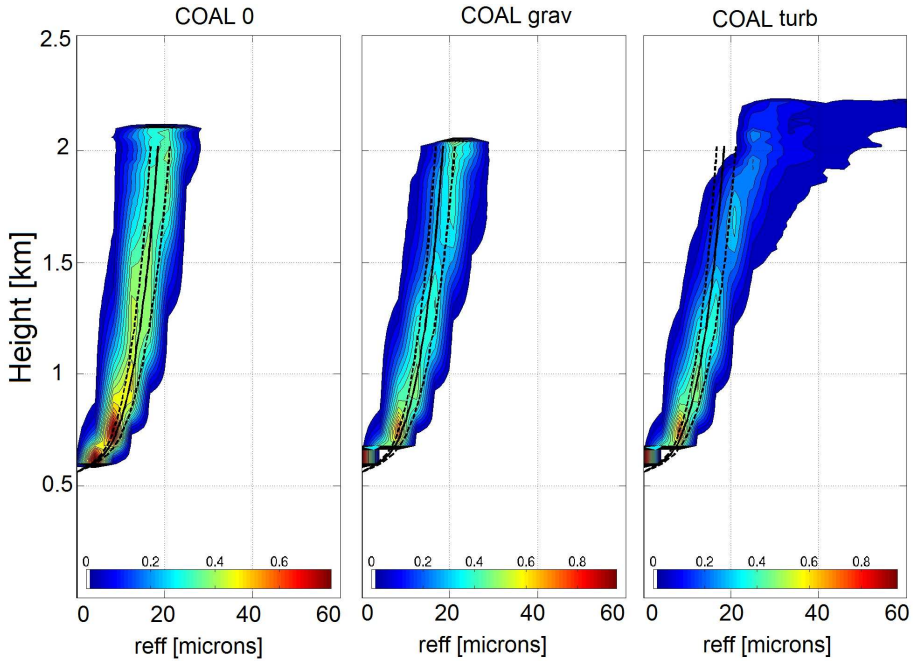

Fig. 8. CFAD of the effective radius (r_{eff}). Solid and dashed lines represent the adiabatic model profiles for the CCN concentration of 120 mg^{-1} and 90/150 mg^{-1}.

ACPD
13, 9217–9265, 2013

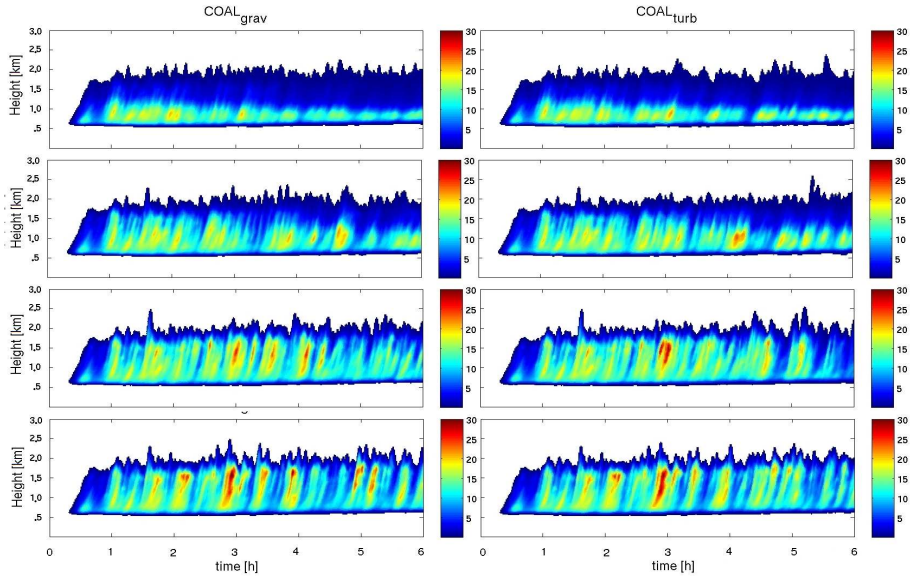

Fig. 9. Time evolution of the horizontally averaged cloud water mixing ratio. Left (right) column shows cases with the gravitational (turbulence-enhanced) kernel. Rows from top to bottom for *N*30, *N*60, *N*120, and *N*240, respectively. Color scale has units of mg kg^{-1}.

ACPD
13, 9217–9265, 2013

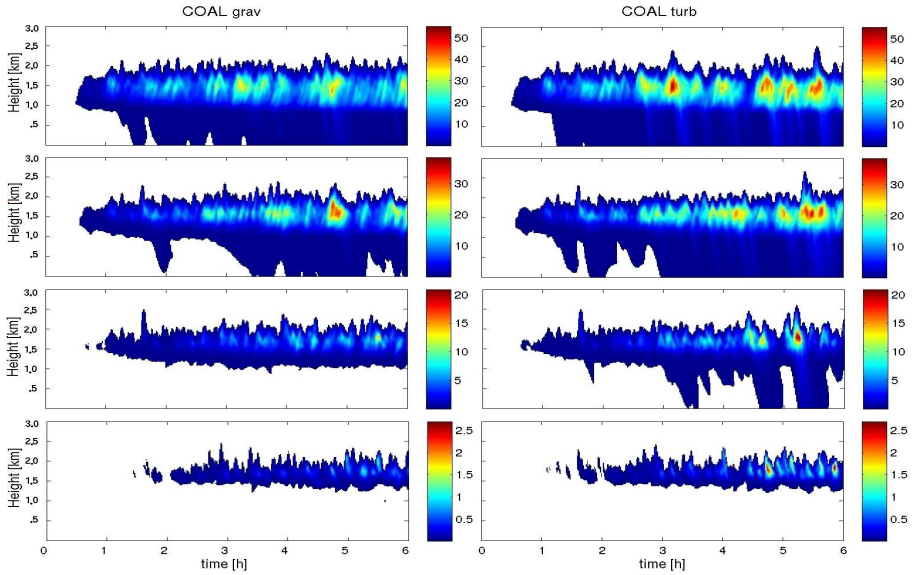

Fig. 10. As in Fig. 9 but for above but for the precipitating (drizzle/rain) water mixing ratio. Color scale has units of mg kg^{-1}.

ACPD
13, 9217–9265, 2013

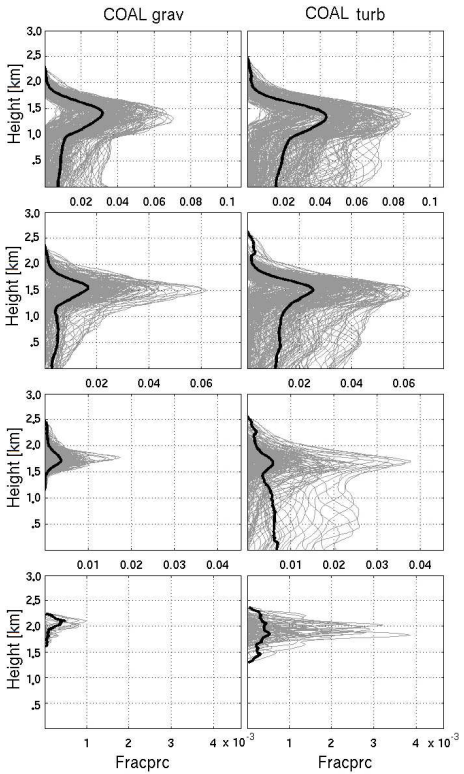

Fig. 11. Profiles of the precipitation fraction (Fracprc) for simulations with (left column) gravitational kernel and (right column) turbulent kernel, and for simulations (top to bottom) *N*30, *N*60, *N*120, and *N*240. Gray lines represent evolution of 1 min average profiles between hours 1 and 6; black thick line is the average of the gray profiles.

ACPD
13, 9217–9265, 2013

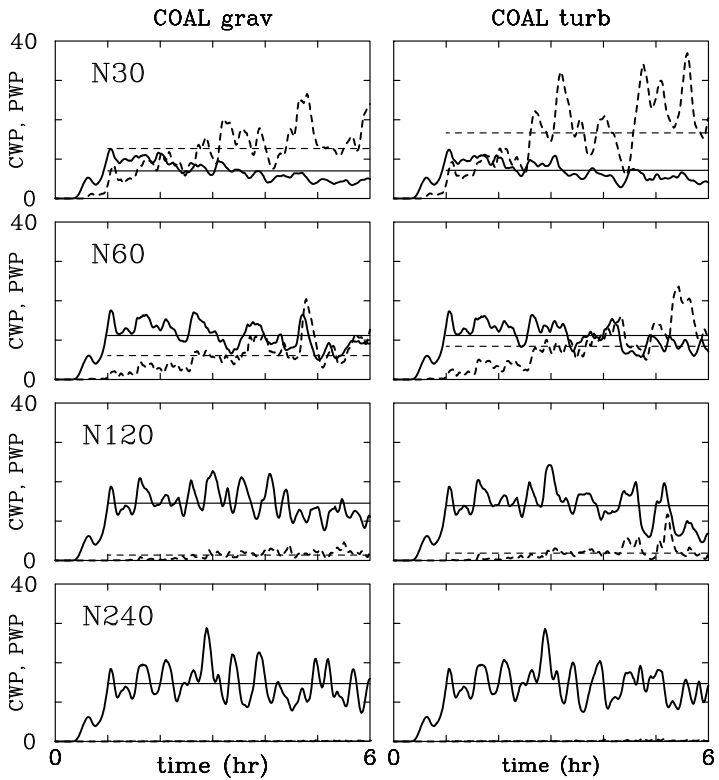

Fig. 12. Evolution of the 1 min domain-averaged CWP (thick solid lines) and PWP (thick dashed lines) for the gravitational (left panels) and turbulent (right panels) kernel simulations *N*30, *N*60, *N*120, and *N*240, from top to bottom, respectively. CWP and PWP is in $\mathrm{g\,m^{-2}}$. The thin solid/dashed lines show 5 h average CWP/PWP between hours 1 and 6 of the simulation.

ACPD
13, 9217–9265, 2013

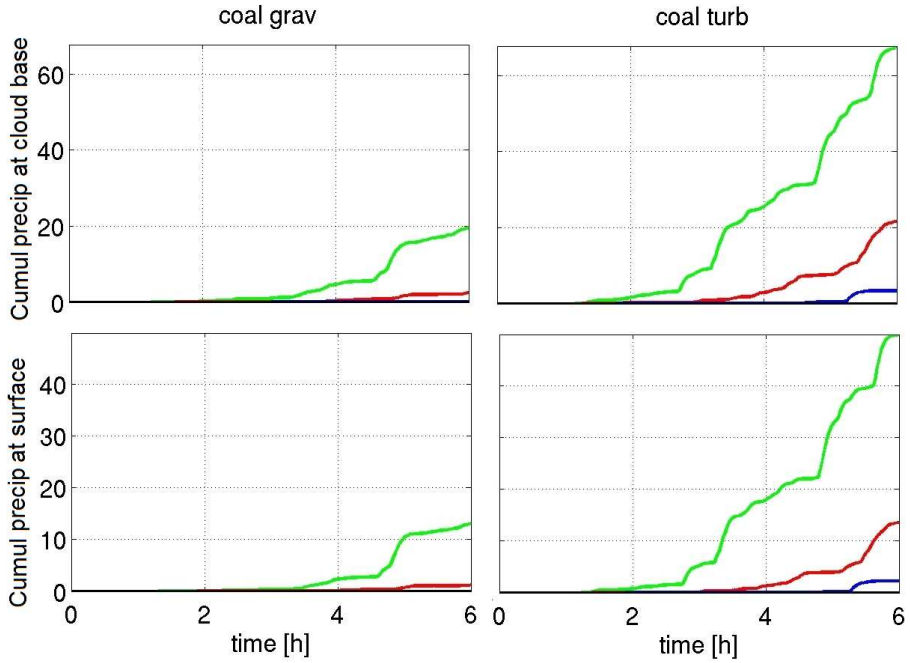

Fig. 13. Evolution of the cumulative precipitation (cumul precip) flux [mm] at the clod base (upper panels) and at the surface (bottom panels) for gravitational (left) and turbulent (right) collection kernels. Green, red and blue lines represent evolutions for *N*30, *N*60, and *N*120 simulations, respectively.

ACPD
13, 9217–9265, 2013

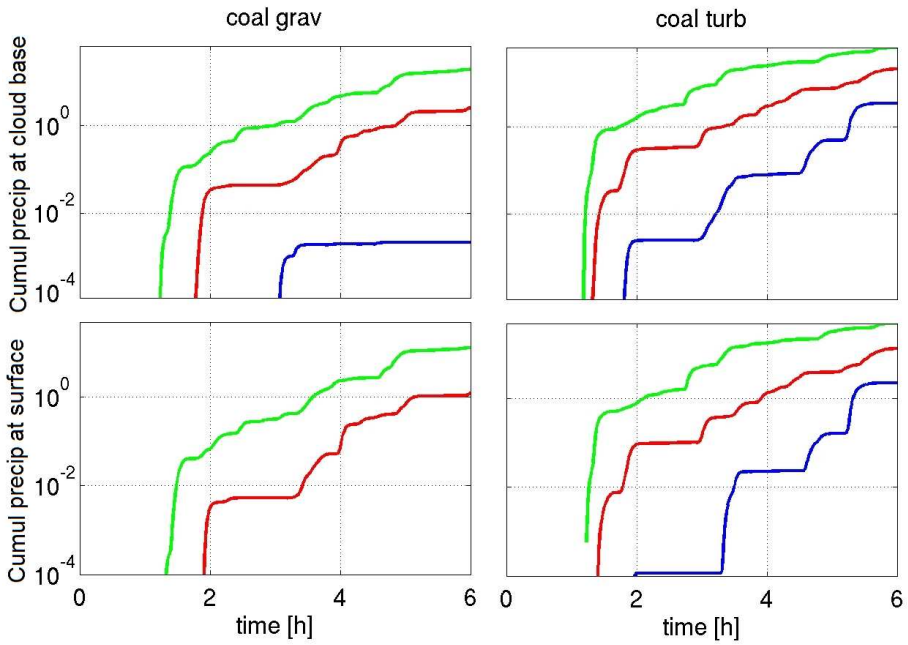

Fig. 14. Same as Fig. 13 but with the logarithmic scale on the vertical axis.

ACPD
13, 9217–9265, 2013